Runout effects in milling: Surface finish, surface location error, and stability

Tony L. Schmitz[a,*], Jeremiah Couey[b], Eric Marsh[b], Nathan Mauntler[a], Duke Hughes[a]

[a]Department of Mechanical and Aerospace Engineering, University of Florida, P.O. Box 116300, 237 MAE-B, Gainesville, FL, 32611, USA
[b]Department of Mechanical Engineering, Penn State University, University Park, PA, USA

Abstract

This paper investigates the effect of milling cutter teeth runout on surface topography, surface location error, and stability in end milling. Runout remains an important issue in machining because commercially-available cutter bodies often exhibit significant variation in the teeth/insert radial locations; therefore, the chip load on the individual cutting teeth varies periodically. This varying chip load influences the machining process and can lead to premature failure of the cutting edges. The effect of runout on cutting force and surface finish for proportional and non-proportional tooth spacing is isolated here by completing experiments on a precision milling machine with 0.1 μm positioning repeatability and 0.02 μm spindle error motion. Experimental tests are completed with different amounts of radial runout and the results are compared with a comprehensive time-domain simulation. After verification, the simulation is used to explore the relationships between runout, surface finish, stability, and surface location error. A new instability that occurs when harmonics of the runout frequency coincide with the dominant system natural frequency is identified.
© 2006 Elsevier Ltd. All rights reserved.

Keywords: Machining; Eccentricity; Dynamics; Simulation; Chatter; Bifurcation

1. Introduction

Radial runout, or eccentricity, of the cutter teeth is a common problem in multiple cutting edge, interrupted machining operations. Well-known effects include premature cutting edge failure due to periodic variations in the chip load and force, as well as increased machined surface roughness. Several previous runout studies are available in the literature. Kline and DeVor introduce the problems associated with radial runout in end milling operations and show the importance of the relationship between the runout and chip load on surface finish [1]. Lazoglu [2] and Feng and Menq [3,4] include runout in ball end milling simulations. Zheng et al. [5] and Baek et al. [6] describe face milling models which consider runout. Atabey et al. detail a boring model that includes runout. [7]. Mezentsev et al. outline a model-based method for fault detection in tapping which includes runout [8]. Altintas and Chan

include runout effects in a chatter suppression scheme for end milling that relies on continuously variable spindle speed [9]. The identification of cutting force coefficients in the presence of runout is described by Wang and Zheng [10], Ko et al. [11], and Yun and Cho [12]. Efforts focused on in-process monitoring and rejection of runout contributions to the cutting force are described by Heckman and Liang [13], Yan et al. [14], Stevens and Liang [15], and Liang and Wang [16]. Additionally, Baek et al. [17] describe an optimum selection of feed rate considering runout in face milling operations.

In this paper, we build on these previous efforts by combining time-domain simulation with a machining setup that allows continuous variation of runout while minimizing other surface roughness contributors, such as spindle and slide error motions. Additionally, we consider endmills with both proportional and non-proportional teeth spacing.[1] The paper is organized as follows: Section 2 provides

---

*Corresponding author. Tel.: +1 352 392 8909; fax: +1 352 392 1071.
E-mail address: tschmitz@ufl.edu (T.L. Schmitz).

[1]Non-proportional teeth spacing can be used to eliminate chatter by interrupting the regeneration of surface waviness (caused by tool

a description of the time-domain simulation; Section 3 describes the setup used to determine the specific cutting energy coefficients for the force model and validate the model; Section 4 presents surface measurements and predictions for cutting conditions that differ from the force model development; Section 5 includes a discussion of the influence of runout on surface finish, stability and surface location error; and Section 6 summarizes the paper.

2. Time-domain simulation description

The time-domain simulation applied in this study is based on the 'Regenerative Force, Dynamic Deflection Model' described by Smith and Tlusty [18], which includes the contribution of the tool/workpiece vibrations to the instantaneous chip thickness, and provides predictions for both force and deflection in the x- and y-directions in the plane of the cut (vibrations along the tool axis, or z-direction, are not considered here). We also model the actual trochoidal motion of the cutter teeth, rather than assuming a circular tool path. Other instances of trochoidal tool path simulations from the literature are provided in Refs. [19–21], for example. Our approach is similar in nature to that described by Campomanes and Altintas [21]; however, the authors did not consider runout in the referenced study. One effect which is not modeled is elastic spring back of the work surface after chip removal. This has been shown to be important in micro-milling, for example, but is not included here [22].

The present milling simulation is carried out by first defining the cutting parameters, including spindle speed, Ω, feed/tooth, f_t, radial and axial depths of cut, a and b, respectively, and the tool geometry, including the number of teeth, N_t, teeth pitch (both proportional and non-proportional spacing are allowed), and radial runout, RO of each tooth (straight teeth were used in the experiments and runout was assumed constant over the low axial depths applied here, although this is not a necessary condition for the simulation). The system dynamics are then defined. These are included as modal mass, m, damping, c, and stiffness, k, values for any number of modes (i.e., degrees-of-freedom) in the x- (feed) and y-directions and are obtained from dynamic, typically impact, tests.

The force and deflection are then determined by numerical integration over small steps in time, $dt = 60/(SR \cdot \Omega)$, where dt is given in s, SR is the number of steps per cutter revolution, and Ω is expressed in rev/min, or rpm. In each time step, the cutter is rotated by an angle, $d\phi = 360/SR$ (in degrees). The current nominal $\{Cx_j, Cy_j\}$ coordinates of each tooth on the cutter are then calculated according to Eq. (1), where r_j is the tooth-dependent cutter radius (including runout, RO_j), ϕ_j is the tooth angle, j is the tooth number (which varies from 1 to N_t), $df = N_t f_t/SR$,

is the incremental feed during the time step dt, and x_{tool} and y_{tool} are the tool center coordinates determined in the previous time step (set equal to zero for the first simulation time step). For the tooth-dependent radius values, the RO_j entries are referenced relative to the tooth with the largest radius (assumed equal to the nominal cutter radius). The RO_j value for this tooth is zero, while the rest are negative (or zero) according to their difference from the largest radius value.

$$Cx_j = r_j \sin \phi_j + df + x_{tool},$$
$$Cy_j = r_j \cos \phi_j + y_{tool}. \tag{1}$$

In order to determine the instantaneous radial chip thickness at each time step of the simulation, the $\{Cx_j, Cy_j\}$ coordinates of the current tooth (i.e., point **C** in Fig. 1) are compared to the surface coordinates during the prior tooth passage at the same angular orientation. However, because we are not applying the circular tool path assumption, it is not required that a data point exist at this angle from the prior pass. Therefore, a search is completed to determine the two points from the previous tooth passage which bound this angle, referred to as points **A** and **B** in Fig. 1. Linear interpolation is then completed to determine point **D**, which lies on the line between point **C** and the cutter origin [23]. The coordinates of point **D**, $\{Dx_j, Dy_j\}$, are provided in Eq. (2):

$$Dx_j = \frac{\tan \phi_j \cdot Ax_j C_1 - \tan \phi_j \cdot Ay_j + \tan \phi_j \cdot Cy_j - Cx_j}{\tan \phi_j \cdot C_1 - 1},$$
$$Dy_j = Ay_j - Ax_j C_1 + Dx_j C_1, \tag{2}$$

where $C_1 = (Ay_j - By_j)/(Ax_j - Bx_j)$. The nonlinearity that is exhibited when the vibration amplitude is large enough that a tooth leaves the cut is included by setting the chip thickness, h_j, equal to zero if

$$\sqrt{(Cx_j - x_{tool})^2 + (Cy_j - y_{tool})^2}$$
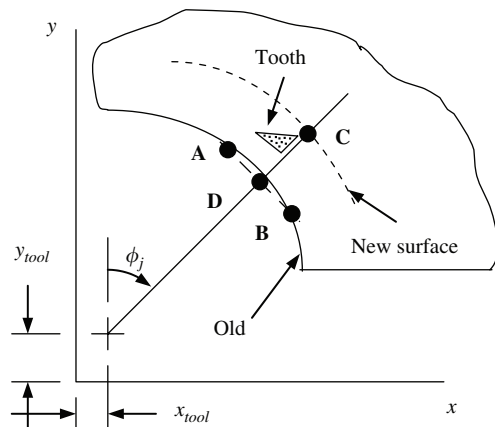$$< \sqrt{(Dx_j - x_{tool})^2 + (Dy_j - y_{tool})^2}. \tag{3}$$

Fig. 1. Determination of instantaneous chip thickness by linear interpolation for trochoidal tool path.

Two other conditions must also be queried for the chip thickness calculation. First, it must be determined if the current tooth is bounded by the specified radial immersion. Second, it must be verified that the chip thickness has not been reduced during cut entry for down milling or cut exit for up milling. The chip thickness reduction that occurs at the cut exit for up milling, for example, is exhibited in Fig. 2.

To determine if the current tooth is bounded by the selected radial depth of cut (i.e., engaged in the cut), the value y_{test}, which gives the y direction coordinate of the desired surface as shown in Fig. 2, is used. For up milling with less than or equal to 50% radial immersion, cutting occurs if Cy_j is greater than y_{test}. This situation is depicted in Fig. 2. If the up milling radial immersion is greater than 50%, then Dy_j must be greater than y_{test} if cutting is to occur (note that y_{test} is negative in this case). For down milling, Cy_j must be less than y_{test} if the radial immersion is less than or equal to 50% and cutting is to take place (y_{test} is again negative). If the radial immersion is greater than 50%, it is required that Dy_j be less than y_{test} if cutting is to occur. In each case, provided the chip thickness is not reduced at the cut exit (up milling) or entry (down milling), as shown in Fig. 2, and the tooth has not vibrated out of the cut (Eq. (3)), h_j is calculated according to Eq. (4):

$$h_j = \sqrt{(Cx_j - Dx_j)^2 + (Cy_j - Dy_j)^2}. \tag{4}$$

To check if the chip thickness reduction condition is met, the tooth coordinates are again compared to y_{test}. The thickness reduction occurs if the following circumstances are satisfied: (1) up milling, less than or equal to 50% radial immersion—Dy_j is less than y_{test}; (2) up milling, greater than 50% radial immersion—Cy_j is less than y_{test}; (3) down milling, less than or equal to 50% radial immersion—Dy_j is greater than y_{test}; and 4) down milling, greater than 50% radial immersion—Cy_j is greater than y_{test}. In these cases, Eq. (4) can no longer be used to compute the instantaneous chip thickness. Rather, point D' identified in Fig. 2 must be considered. The coordinates of this point, $\{Dx'_j, Dy'_j\}$, are provided in Eq. (5).
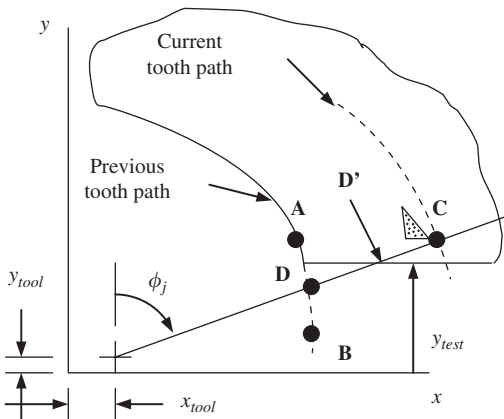
$$Dx'_j = (y_{\text{test}} - y_{\text{tool}}) \tan \phi_j + x_{\text{test}},$$
$$Dy'_j = y_{\text{test}}. \tag{5}$$

Under these conditions, the chip thickness is then calculated using Eq. (6) for up or down milling with less than or equal to 50% radial immersion or Eq. (7) for greater than 50% radial immersion.

$$h_j = \sqrt{(Cx_j - Dx'_j)^2 + (Cy_j - Dy'_j)^2}. \tag{6}$$

$$h_j = \sqrt{(Dx'_j - Dx_j)^2 + (Dy'_j - Dy_j)^2}. \tag{7}$$

In any case that the computed chip thickness is greater than zero, the tangential and radial force components, $F_{\text{tan},j}$ and $F_{\text{rad},j}$, respectively, for tooth j are calculated according to Eq. (8):

$$F_{\text{tan},j} = K_{\text{tc}}bh_j + K_{\text{te}}b,$$
$$F_{\text{rad},j} = K_{\text{rc}}bh_j + K_{\text{re}}b, \tag{8}$$

where K_{tc} and K_{rc} are the force model cutting coefficients and K_{te} and K_{re} are the edge coefficients [24]. We presume that these coefficients indirectly account for complicated tool–chip formation effects such as work hardening and flow stress temperature sensitivity, but have not modeled these effects directly. The forces are summed over all teeth engaged in the cut at the given instant in time. The total forces, $F_{\text{tan}} = \sum_{j=1}^{N_t} F_{\text{tan},j}$ and $F_{\text{rad}} = \sum_{j=1}^{N_t} F_{\text{rad},j}$, are then projected into the x- and y-directions using Eq. (9). These force values are then used to determine the instantaneous displacement values x_{tool} and y_{tool} for the next time step using numerical integration and the measured modal parameters. If multiple vibration modes are included, the displacement contributions from each mode are summed to determine the total displacement. Provided the modal parameters were determined from a direct frequency response function measurement (or model), the same forces are used for each vibration mode.

$$F_x = -F_{\text{tan}} \cos \phi_j - F_{\text{rad}} \sin \phi_j,$$
$$F_y = F_{\text{tan}} \sin \phi_j - F_{\text{rad}} \cos \phi_j, \tag{9}$$

In the case of a helical cutting edge, the tool can be segmented along its axis into several disks, each of which is treated as having a zero helix angle [24,25]. The forces for each disk are then summed to determine the total radial and tangential cutting force components for that particular simulation time step. Eq. (9) is then applied to project the forces in the x- and y-directions and the numerical integration is completed. The difference, $\Delta\phi$ (in deg), between the tooth angle, ϕ_j, for tooth j on disk k and the angle for the same tooth j on disk $k+1$ (located farther away from the tool tip by a distance b/SA) is provided in Eq. (10):

Fig. 2. Reduced instantaneous chip thickness at cut exit in up milling.

$$\Delta\phi = \frac{2b \tan \beta}{SA \cdot d} \cdot \frac{180}{\pi}, \tag{10}$$

where β is the helix angle, SA is the number of axial disks, and d is the nominal cutter diameter. The reader may also note that the runout variable may be represented as a matrix where the entries represent a tooth runout value for each axial disk.

3. Experimental setup for force model validation

Experiments for this work were carried out on a two-axis Moore 450 computer numerically-controlled machining center with a programmable resolution of 0.1 μm and a Professional Instruments 4R Twin Mount air bearing milling spindle with 20 nm-level error motions [26]. See Fig. 3. This machine and air bearing spindle were specifically selected to avoid the typical convolution between spindle error motions and tool runout [27]. In the experiments reported here, because the spindle error motions are one –three orders of magnitude smaller than the prescribed tool runout values, we can assume the runout is constant with spindle speed and dependent only on the tool runout, although this is not the case in general for high-speed rolling element bearing spindles. The cutting forces were recorded using a Kistler mini-dynamometer (Type 9256A2) with a 2 mN resolution. The three force components were recorded using a DSPT Siglab unit at a sampling frequency of 5.12 kHz. Fig. 3 also shows the angle plate used to support the dynamometer and 6061-T6 aluminum workpieces. The cutting tool was an SGS 12.7 mm diameter, two straight flute end mill (proportional teeth spacing) heat shrunk into an aluminum chuck that was precision ground in assembly and subsequently dynamically balanced. Alumicut oil coolant was sprayed onto the cutting tool during cutting.

The custom designed end mill chuck allowed the flute-to-flute radial runout to be varied from 0 to 400 μm by loosening the chuck flange bolts and manually adjusting the assembly to the desired runout value. The runout was measured using an air bearing capacitance probe with a diamond stylus (i.e., the air bearing supported a follower with a diamond stylus that contacted the cutting tool during manual rotation—the capacitance probe sensed the displacement of the follower). Fig. 4 shows the 25 μm/V Lion Precision air bearing capacitance probe setup (the rigid probe holder is not shown). As noted in the figure, the
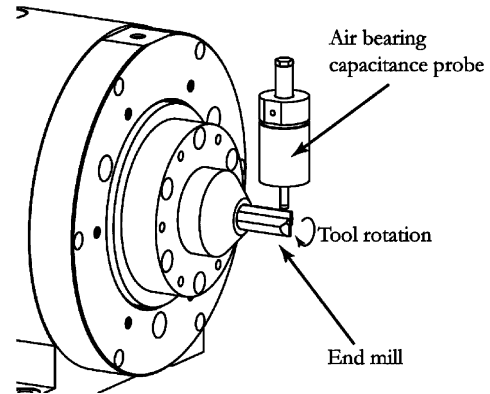

Fig. 4. End mill radial runout measurement using capacitance probe setup.
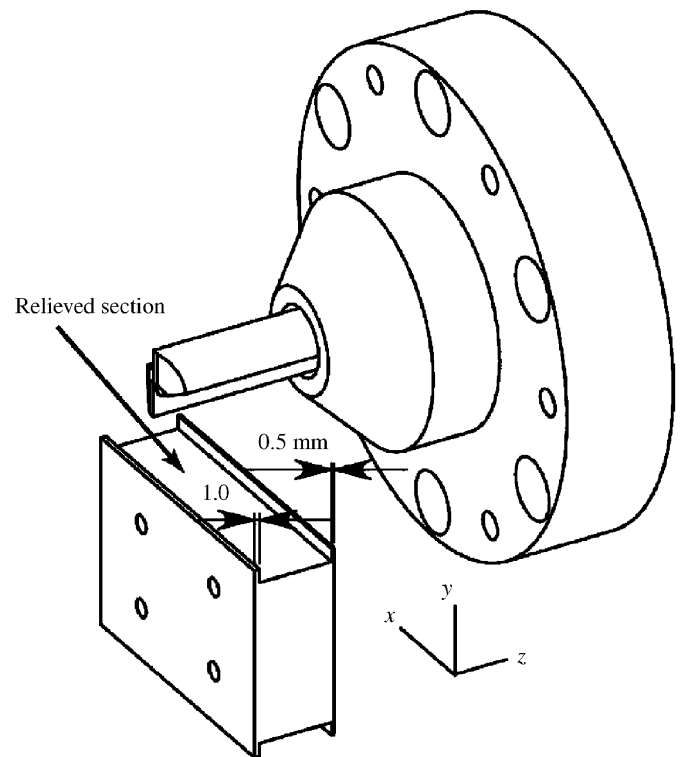

Fig. 5. Dynamometer-mounted workpiece (dynamometer not shown). Peripheral up milling was completed by machining the top of the front raised edge. The workpiece was repositioned to complete four tests with a single sample.
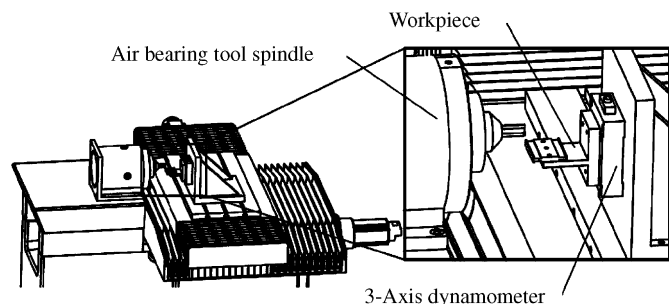
tool was rotated by hand opposite the cutting direction. The runout was then determined by differencing the peak displacement values recorded for the two teeth.

Two workpiece geometries and mounting configurations were used in the cutting tests. First, $33 \times 48 \times 16$ mm samples were mounted directly on the dynamometer. The reversible, relieved geometry shown in Fig. 5 was used to allow pure peripheral up milling with nominal axial depths of 0.5 and 1.0 mm and a nominal radial depth of 1.27 mm (10% radial immersion). Second, $38.1 \times 50.8 \times 6.35$ mm samples were mounted to a *T*-shaped base as shown in Fig. 6. Again, the relieved geometry enabled pure

Fig. 3. Two-axis milling machine with air bearing spindle. The dynamometer and *T*-base mount with workpiece are also shown.
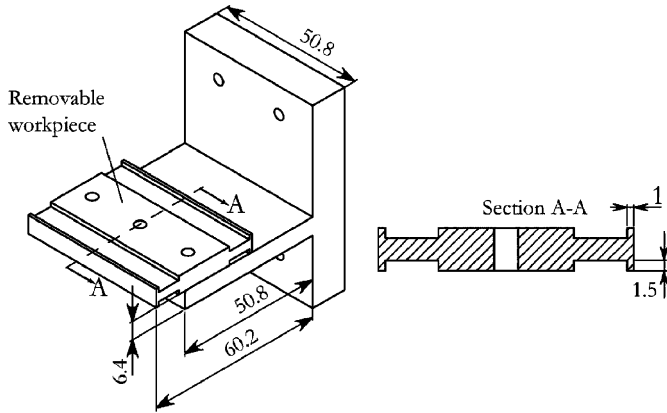
Fig. 6. T-base workpiece mount. The assembly dynamic stiffness was significantly less than the tool. Four tests were completed on each sample.

Table 1
Experimental cutting coefficients.

K_{tc} (N/mm²)	K_{rc} (N/mm²)	K_{te} (N/mm)	K_{re} (N/mm)
1000	520	2	3

peripheral up milling. This base-workpiece assembly was significantly more flexible than the cutting tool (natural frequency, $f_n = 1075$ Hz, $k = 1.1 \times 10^6$ N/m, damping ratio, $\zeta = 0.009$ determined by impact testing); modal parameters were determined by impact testing and least squares polynomial curve fitting and used to define the dynamics in simulation.

To enable comparison between experimental and simulated results, the four coefficients for the force model shown in Eq. (8) were determined experimentally using the mechanistic identification procedure described by Altintas [24]. In this approach, slotting cuts with constant axial depth were made in the rigid workpieces over a range of feed/tooth values. The average force/tooth is recorded and the four cutting coefficients are identified by a linear regression of feed/tooth vs. average force. In our tests, the axial depth was 1.0 mm, the feed/tooth values were {0.02, 0.04, 0.06, 0.08} mm/tooth, and the spindle speed was 5290 rpm. The average force per tooth was determined by sectioning the digital cutting force data into single tooth passages using a once-per-revolution capacitance probe signal (also recorded during cutting at 5.12 kHz). The cutting coefficients are provided in Table 1. These cutting force values are somewhat higher than would be expected for 6061-T6 aluminum. This may be due to the straight flute geometry or the cutting edge preparation for the tools used in this study (i.e., increased cutting forces for small feed/tooth values due to the non-zero cutting edge radius). The reader may note that predictions for much higher or lower feed/tooth values could require additional testing to identify any dependence of the cutting coefficients on the nominal feed per tooth. Cutting tests for both mounting configurations were completed at three different runout
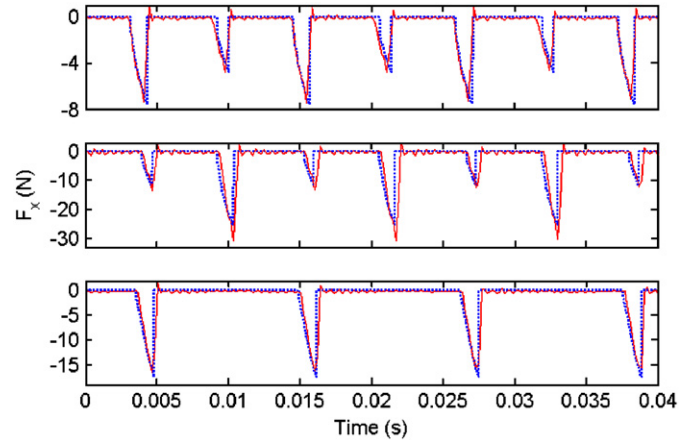

Fig. 7. Dynamometer mount measured (solid line) and simulated (dotted line) x-direction force data: (top) RO = 2 μm; (middle) RO = 4.9 μm; (bottom) RO = 33 μm. Note changes in force axis scales.

values: {2, 4.9, and 33} μm. Comparisons between measured and simulated x-direction forces for the dynamometer mount are shown in Fig. 7. The cutting conditions for the three panels were: (top) $f_t = 0.01$ mm/tooth, RO = 2.0 μm, $a = 1.245$ mm, $b = 0.635$ mm; (middle) $f_t = 0.02$ mm/tooth, RO = 4.9 μm, $a = 1.168$ mm, $b = 1.194$ mm; and (bottom) $f_t = 0.02$ mm/tooth, RO = 33 μm, $a = 1.524$ mm, $b = 0.572$ mm (the reader may note that for this RO value, only a single tooth is engaged in the cut). Comparable agreement was seen for y direction data, but has not been included here for brevity.

In order to make a direct comparison with forces measured using the T-base (flexible)-workpiece assembly shown in Fig. 6, the simulated data was filtered by the dynamometer force-to-cutting force frequency response [28]. This response was obtained by exciting the free end of the T-base-workpiece assembly with an impact hammer and recording both the hammer input and the dynamometer force output. The resulting dynamometer force-to-cutting force frequency response was least squares fit with a 2nd-order (in both the numerator and denominator) filter, $F_{dynamometer}/F_{cutting}(\omega)$, and used to correct the simulated force according to Eq. (11), where $F_{y,d}(\omega)$ is the frequency-domain filtered force. This result was then inverse Fourier transformed to obtain the new simulated force that was compared to the measured y direction force. A 2nd-order fit to the required frequency response was applied because it exhibited a single mode at the T-base-workpiece fundamental clamped-free natural frequency within the bandwidth of interest (5 kHz).

$$F_{y,d}(\omega) = \frac{F_{dynamometer}}{F_{cutting}} \cdot F_y, \qquad (11)$$

Comparisons between measured and simulated y direction forces for the T-base mount with the Eq. (11) filtering applied are shown in Fig. 8. The cutting conditions for the three panels were: (top) $f_t = 0.02$ mm/tooth, RO = 2.0 μm,
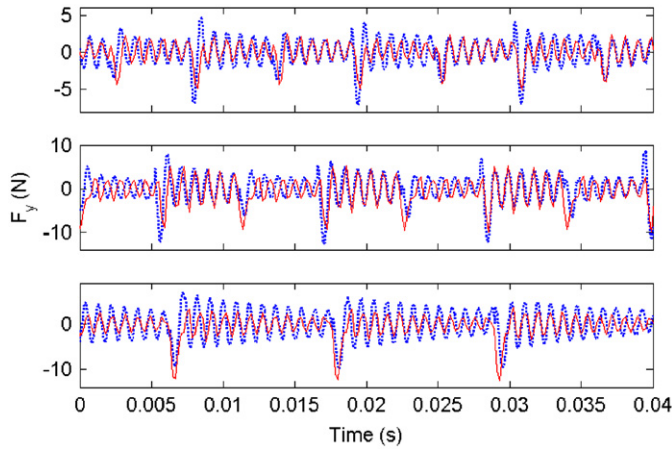
Fig. 8. *T*-base mount measured (solid line) and simulated (dotted line) *y* direction force data with dynamics correction: (top) RO = 2 μm; (middle) RO = 4.9 μm; and (bottom) RO = 33 μm. Note changes in force axis scales.

$a = 1.295$ mm, $b = 0.584$ mm; (middle) $f_t = 0.02$ mm/tooth, RO = 4.9 μm, $a = 1.124$ mm, $b = 1.054$ mm; and (bottom) $f_t = 0.02$ mm/tooth, RO = 33 μm, $a = 1.461$ mm, $b = 1.041$ mm (again, for this runout value only a single tooth is cutting). The agreement between the measured and simulated results is reasonable, but less accurate than the *x*-direction data shown in Fig. 7. The reason for the discrepancy is due to the difficulty of measuring the dynamics without influencing the system under test. Also, the fixture design led to slight variation in the workpiece mounting between the multiple cutting tests. Impact tests showed up to a 20 Hz shift in the assembly natural frequency under different mounting conditions, primarily due to clearance in the workpiece through holes (see Fig. 6). For the simulated forces in Fig. 8, the modal parameters for an average frequency response function were used to predict all cases.

4. Surface prediction and measurement

Once the force model was verified on both rigid and flexible workpieces, comparisons were made between machined and simulated surfaces using: (1) the previously-defined two flute, straight tooth cutter; and (2) a modified 12.7 mm diameter Woodruff cutter. Originally, the Woodruff cutter had 12 proportionally-spaced teeth (located at $\{0, 30, 60, \ldots, 330\}°$). However, 10 of the straight teeth were ground away to leave cutting edges only at the 0° and 210° orientations. The cutter was then mounted in the chuck and dynamically balanced to minimize the influence of forced vibrations (due to mass imbalance) on the machined surfaces. Different cutting conditions were used for the surface prediction tests than for the force model validation to demonstrate the generality of the simulation model. The sample surface finish was recorded using a Wyko NT 1000 non-contact interfero-

metric profiler (i.e., a scanning white light interferometer) using a $2.5\times$ objective with a 1.9×2.5 mm field of view. Once the surface finish topograph was collected for each cutting condition, a line trace was then extracted from the center of the surface profile for direct comparison to simulation.

4.1. Proportional teeth spacing results

The surface finish of the flexible workpieces was compared to the predicted results for up milling using the two flute, straight tooth cutters with: $a = 0.5$ mm; $b = 0.5$ mm; $f_t = \{0.51$ and $0.24\}$ mm/tooth; and $\Omega = \{150$ and $300\}$ rpm. The runout values varied between 0.3 and 37 μm. A progression of representative results is shown in the four panels provided in Fig. 9. In all cases, the experimental results are represented by the heavy solid line, while the simulated tool path is given by the lighter solid and dotted lines, where the dotted line represents the tooth with a smaller radius (i.e., lower runout value). In panel (a), the combination of small runout and lower feed per tooth gives the expected cusped surface with a spatial period nominally equal to the feed/tooth. As the runout is increased to 5 μm while the feed/tooth is held constant, the surface is defined only by the larger radius tooth as shown in panel (b). In panel (c), the runout is slightly smaller, 4.2 μm, but the feed/tooth has been doubled. Now the surface is left by the combination of both teeth; however, the spatial period is not constant, but varies from one tooth to the next. Panel (d) shows the result for a 33 μm runout; again, only one tooth leaves the final surface. As expected, the spatial period doubles between panels (b) and (d). In all cases, good agreement is seen between
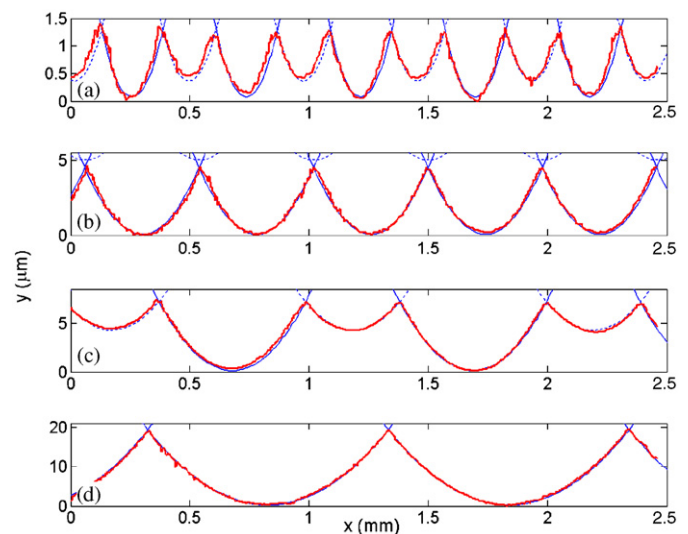

Fig. 9. Two flute, straight tooth cutter: (a) $ft = 0.24$ mm/tooth, $\Omega = 300$ rpm, RO = 0.3 μm; (b) $ft = 0.24$ mm/tooth, $\Omega = 300$ rpm, RO = 5 μm; (c) $ft = 0.51$ mm/tooth, $\Omega = 150$ rpm, RO = 4.2 μm; and (d) $ft = 0.51$ mm/tooth, $\Omega = 150$ rpm, RO = 33 μm.

experiment and simulation (the reader may note the difference in vertical scales between the four panels).

4.2. Non-proportional teeth spacing results

The up milling cutting conditions for the flexible workpiece cutting trials and simulations using the non-proportional Woodruff cutter were: $a = 1.0$ mm; $b = 0.65$ mm; $f_t = \{0.36$ and $0.19\}$ mm/tooth; and $\Omega = \{200$ and $400\}$ rpm. The runout values varied between 2.4 and 32 μm. Example results for the 400 rpm tests are provided in Fig. 10. It is seen that the surface topography changes very little between the three panels (note that the scales are equal). This is because, even for the smallest runout value of 2.4 μm, the surface is generated predominantly by a single tooth. This result underscores the importance of minimizing runout in situations that require low surface roughness.
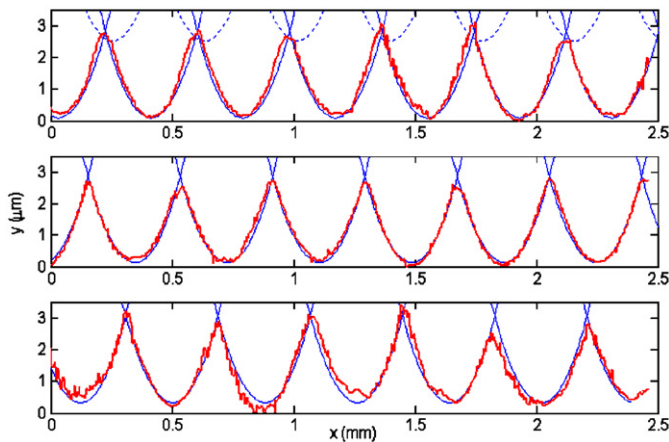

Fig. 10. Woodruff cutter with $ft = 0.19$ mm/tooth and $\Omega = 400$ rpm: (top) RO = 2.4 μm; (middle) RO = 5.5 μm; and (bottom) RO = 32 μm.
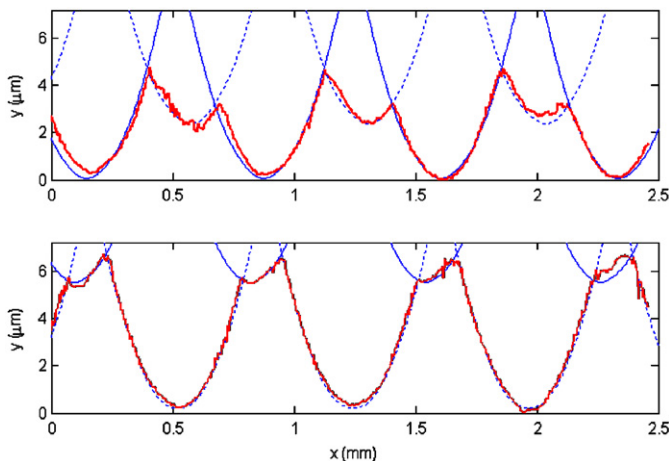

Fig. 11. Woodruff cutter with $ft = 0.36$ mm/tooth and $\Omega = 200$ rpm: (top) RO = 2.4 μm, radius for 0° tooth is largest; and (bottom) RO = 5.5 μm, radius for 210° tooth is largest.

Fig. 11 shows results for two 200 rpm tests. In the top panel, the radius of the tooth oriented at 210° was 2.3 μm less than the tooth at 0°. The 0° tooth (solid line) primarily creates the surface, while the 210° tooth removes a portion of the cusp off-center to the right. In the bottom panel, the 210° tooth had the larger radius (5.5 μm runout). The surface is now generated mainly by the 210° tooth and the 0° tooth removes a portion of the cusp off-center to the left. The axis scales are again equal in the two panels.

5. Discussion

Once the simulation force and surface finish predictions were verified experimentally, the code was used to explore the global effects of runout on surface roughness, stability, and surface location error.

5.1. Surface roughness analysis

The first task was to organize the surface roughness prediction information into a useable format. Our intent was to collect the 'local view' of the process available from time-domain analysis into a 'global view' that could be conveniently used by process planners. Because the surface texture coefficients described in ASME B46.1-2002 are commonly used to express the surface finish requirements on engineering drawings, we focused our attention on the common metric referred to as roughness average, Ra [29]. The reader may note that we have assumed constant cutting force coefficients for all simulations. Practically, it may be necessary to vary these coefficients as a function of feed/tooth and/or cutting speed to accurately capture the complicated tool–chip interactions over a broad range of cutting conditions.

Fig. 12 exhibits the relationship between Ra, f_t, and runout for the two flute, straight tooth cutter with proportional tooth spacing. As expected, the tendency is toward higher roughness values with increases in f_t, and runout. However, closer examination shows counterintuitive local trends. Fig. 13 shows contours of constant Ra values as a function of feed/tooth and radial runout (i.e., the planar projection of Fig. 12). It is seen that the roughness average does not increase monotonically with f_t, and runout. Rather, for a constant feed per tooth (see the vertical line in Fig. 13), Ra is seen to increase and then decrease as the runout becomes larger. The information in Fig. 13 allows a process planner to view the trade-off between runout and surface roughness. For a priori knowledge of the runout, the maximum feed/tooth value that satisfies the surface quality requirements can be selected.

5.2. Stability analysis

Next, simulated Ra data was collected into a map similar to the well-known stability lobe diagram, which identifies stable and unstable cutting zones as a function of spindle
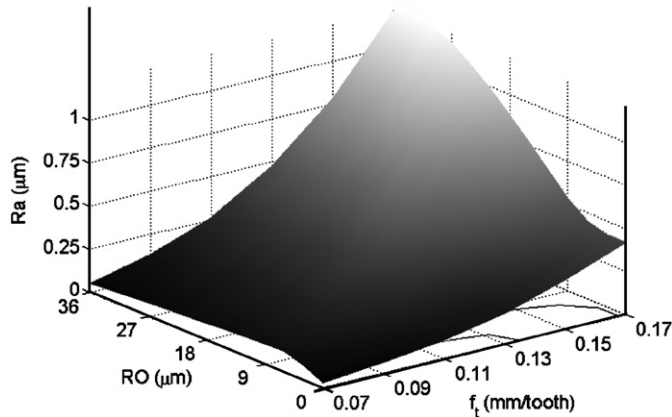
Fig. 12. Simulated roughness average (*Ra*) as a function of the feed/tooth (*ft*) and runout (RO). As expected the roughness increases with RO and *ft*.
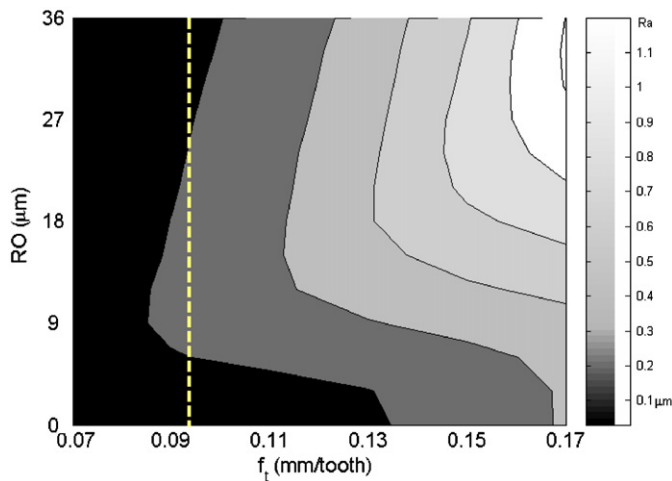

Fig. 13. Contour plot of simulated roughness average (*Ra*) as a function of the feed per tooth (*ft*) and runout (RO). It is seen that increasing the RO does not continuously increase the *Ra* (heavy dotted line).

speed and chip width (axial depth of cut in peripheral end milling operations). Fig. 14(a) shows the analytical stability boundary for a 50% radial immersion down milling cut [30]. Simulation parameters were: 25.4 mm diameter, four flute end mill (proportional teeth spacing with 30° helix angle) with no runout; a single vibration mode in the *x*- and *y*-directions ($f_n = 500$ Hz, $k = 1 \times 10^7$ N/m, $\zeta = 0.01$); $K_{tc} = 700$ N/mm², $K_{rc} = 210$ N/mm², $K_{te} = K_{re} = 0$; and $f_t = 0.1$ mm/tooth. Fig. 14(b) shows lines of constant *Ra* as a function of spindle speed and axial depth.[2] Clearly, the contour plot captures the stability behavior. However, rather than identifying the stability boundary as a single line, or step function, the transition from unstable to stable behavior is shown in a more usable fashion for process planners. Based on this diagram, once the desired surface roughness is known, the cutting conditions can be deterministically selected to achieve the

required surface finish without sacrificing high material removal rates.

5.3. Surface location error analysis

It is well known that time-domain simulation can be applied to the computation of surface location error, or part geometric error that arises from forced vibration of the cutting tool. However, to the authors' knowledge, the effect of runout on surface location error has not been explored in the literature.

The surface location error amplitude depends on the position of the cutter as it leaves the surface (i.e., as it exits the cut in down milling or enters the cut in up milling). This position, in turn, depends on the frequency of forced oscillations, which is defined by the tooth passing frequency (or spindle speed). Surface location error is, therefore, spindle speed dependent. The largest variation in surface location occurs when the fundamental tooth passing frequency (or one of its harmonics) is near the natural frequency, f_n (in Hz), which corresponds to the most flexible structural vibration mode. These 'sensitive speeds', Ω_s in rpm, are defined in Eq. (12). The reader may note that these are the same speeds selected to take advantage of the peaks in the stability lobes as seen in Fig. 14.

$$\Omega_s = \frac{60 \cdot f_n}{j \cdot N_t}, \quad j = 1, 2, 3, \ldots. \tag{12}$$

In the presence of runout, additional frequency content is observed at the spindle rotational frequency (or runout frequency) and its harmonics. Therefore, it should be expected that supplementary sensitive speeds will exist where the runout frequency or its harmonics are near f_n. This will also serve to excite the structural dynamics. The full complement of Ω_s values for a two flute cutter can then be expressed as shown in Eq. (13), where the bottom equation identifies the runout-dependent speeds.

$$\Omega_s = \begin{cases} 60 \cdot f_n/j \cdot N_t \\ 60 \cdot f_n/2j - 1 \end{cases}, \quad j = 1, 2, 3, \ldots. \tag{13}$$

To test these sensitive speeds, simulations were carried out for the following conditions: 10% radial immersion down milling; 12.7 mm diameter, two flute end mill (proportional teeth spacing with 30° helix angle); a single vibration mode in the *x*- and *y*-directions ($f_n = 500$ Hz, $k = 1 \times 10^7$ N/m, $\zeta = 0.01$); $K_{tc} = 700$ N/mm², $K_{rc} = 210$ N/mm², $K_{te} = K_{re} = 0$; $f_t = 0.1$ mm/tooth; and a 3.0 mm axial depth of cut (well below the critical stability limit of 4.6 mm—see Fig. 17—so that stable cuts should be observed at all spindle speeds). The spindle speed was varied over the range from 5000 to 30 000 rpm in increments of 50 rpm and the runout was 20 µm. For this spindle speed range, the sensitive spindle speeds from Eq. (13) are: {30 000, 10 000, 6000, …} rpm for the runout frequency content and {15 000, 7500, 5000, …} rpm for the

---

[2]A similar plot can be found in Ref. [33], but the ratio of the simulated roughness to theoretical (geometric) roughness was presented.
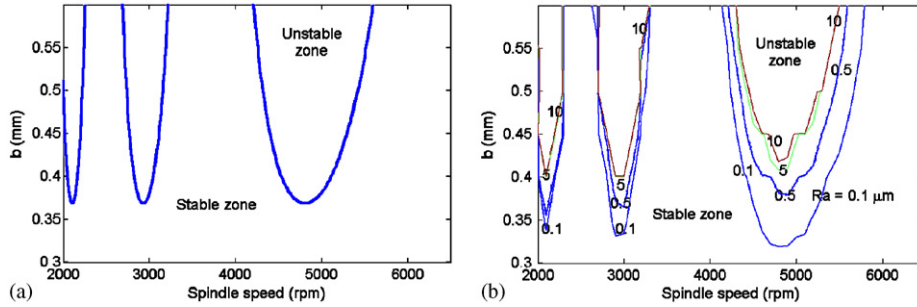
Fig. 14. (a) Analytical stability lobe diagram for 50% radial immersion down milling cut. (b) Lines of constant *Ra* from time-domain simulation.
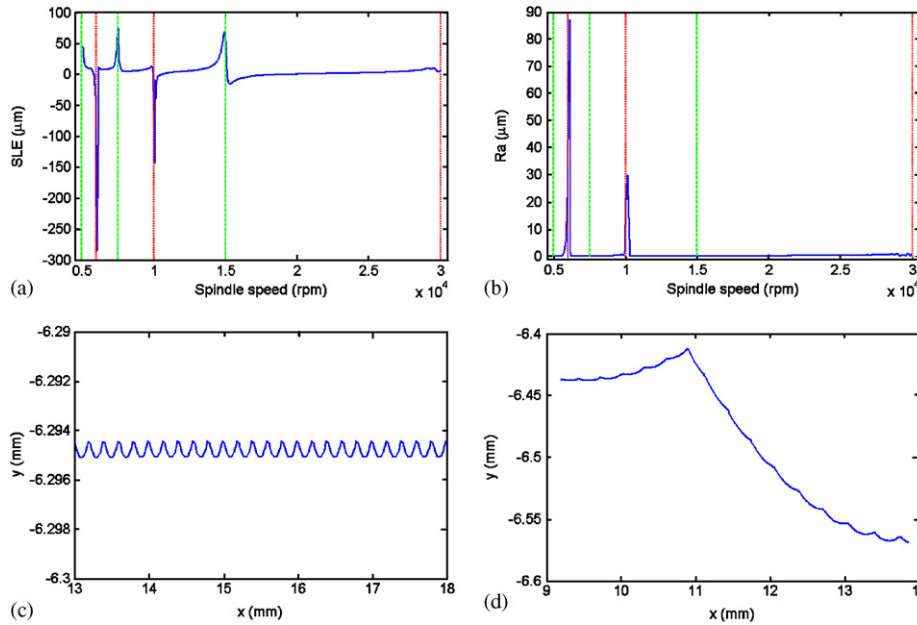

Fig. 15. (a) Surface location error (SLE) versus spindle speed. Variations in the machined surface position are seen when: (1) the tooth passing frequency or its harmonics are near *fn* (dashed lines); and (2) when the runout frequency or its harmonics are near *fn* (dotted lines). (b) *Ra* versus spindle speed. Poor surface finish is observed when the runout frequency first and third harmonics are near *fn*; (c) surface profile at 15 000 rpm—the final surface location is in error by +55 µm relative to the commanded location (−6.35 mm), but the cut is stable (*Ra* = 0.2 µm); (d) surface profile at 10 000 rpm—the cut is now unstable (SLE = −133 µm, *Ra* = 30 µm).

tooth passing frequency content. The simulation results are shown in Fig. 15.

In Fig. 15(a) the traditional periodic variation in surface location as the tooth passing frequency and its harmonics pass through f_n is observed (sensitive speeds identified by the dashed lines). Runout has no appreciable effect at these speeds. However, strong sensitivity of the error to spindle speed is also observed when the third and fifth runout harmonics are near f_n (dotted lines). Fig. 15(b) shows that the surface roughness is also high near these speeds. The surface profiles for 15 000 and 10 000 rpm simulations are provided in panels Figs. 15(c) and (d), respectively. It is seen that the *Ra* and surface location error values are significantly higher for the 10 000 rpm case.

To better understand these small regions of large error, results for a single time-domain simulation completed at 10 050 rpm are shown in Fig. 16. Here, the instability resembles the period-doubling instability (i.e., flip bifurcation) first reported by Davies et al. [31], but it occurs at different spindle speeds; the large *y* direction oscillations occur at $f_n = 500$ Hz. Note that the cut would be stable if no runout were present. It can also be observed that the cut is stable with small surface location error when the fundamental runout frequency is near f_n (∼30 000 rpm). In this case, all runout and tooth passing frequency harmonics are located to the right of f_n. However, for the 10 050 rpm case, the runout third harmonic near f_n is accompanied by the fundamental tooth passing frequency on the left and its first harmonic on the right. The combined forcing frequency content would appear to contribute to the local instability(s) observed in Figs. 15 and 17.
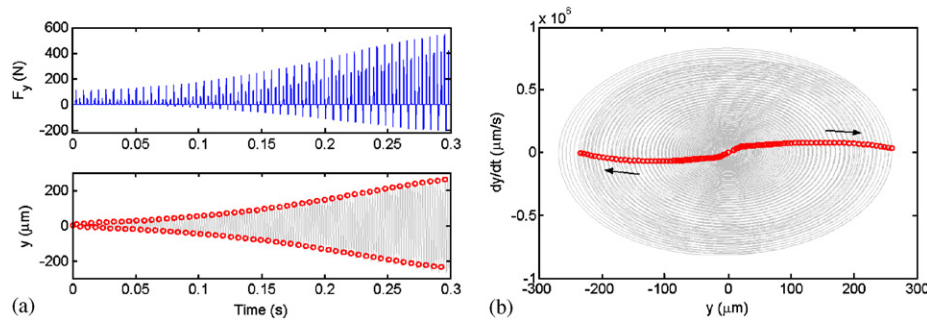
Fig. 16. (a) Force and displacement in the *y* direction. The displacement is sampled at the tooth passing frequency (circles) and the instability is observed. (b) Phase space representation of *y* displacement versus velocity. The 1/tooth sampled points occur on two diverging trajectories.
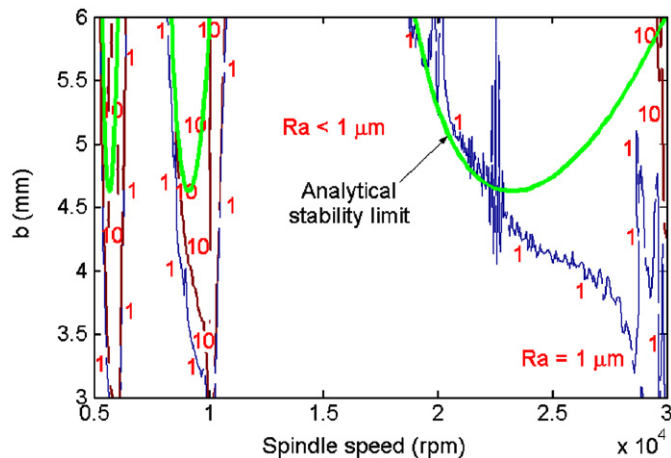

Fig. 17. Analytical stability limit and lines of constant *Ra* for 10% radial immersion down-milling two flute cutter with 20 μm runout. It is seen that significant increases in surface roughness occur below the critical stability limit (4.6 mm) at the runout frequency-based sensitive speeds.

The results for axial depths from 3 to 6 mm for the same cutting conditions are provided in Fig. 17. For the 20 μm runout, it is seen that the surface roughness is high (indicating instability) for axial depths below the critical stability limit (4.6 mm) at the runout frequency-based sensitive speeds (10 000 and 6000 rpm).

6. Conclusions

In this paper, time-domain milling simulation results, which observed the trochoidal motion of the cutter teeth, were compared to experimental cutting force values and surfaces for cutters with proportional and non-proportional teeth spacing over a range of runout values and cutting conditions. The runout effects were isolated by completing experiments on a precision milling machine with 0.1 μm positioning repeatability, 0.02 μm spindle error motion, and continuously variable runout. Using the verified simulation, the graphical relationship between surface roughness, runout, and feed/tooth was provided and it was shown that local decreases in the surface roughness for a constant feed/tooth can occur as the runout is varied. Additionally, new regions of instability

that occur in the presence of runout when harmonics of the runout frequency coincide with the system natural frequency were demonstrated.

References

[1] W.A. Kline, R.E. DeVor, The effect of runout on cutting geometry and forces in end milling, International Journal of Machine Tool Design and Research 23 (2–3) (1983) 123–140.

[2] I. Lazoglu, Sculpture surface machining: a generalized model of ball-end milling force system, International Journal of Machine Tools and Manufacture 43 (5) (2003) 453–462.

[3] H.-Y. Feng, C.-H. Menq, The prediction of cutting forces in the ball-end milling process—I. Model formulation and model building procedure,, International Journal of Machine Tools and Manufacture 34/5 (1994) 697–710.

[4] H.-Y. Feng, C.-H. Menq, The prediction of cutting forces in the ball-end milling process—II. Cut geometry analysis and model verification, International Journal of Machine Tools and Manufacture 34 (5) (1994) 711–719.

[5] H.Q. Zheng, X.P. Li, Y.S. Wong, A.Y.C. Nee, Theoretical modeling and simulation of cutting forces in face milling with cutter runout, International Journal of Machine Tools and Manufacture 39 (12) (1999) 2003–2018.

[6] D.K. Baek, T.J. Ko, H.S. Kim, A dynamic surface roughness model for face milling, Precision Engineering 20 (3) (1997) 171–178.

[7] F. Atabey, I. Lazoglu, Y. Altintas, Mechanics of boring processes—Part II. Multi-insert boring heads, International Journal of Machine Tools and Manufacture 43 (5) (2003) 477–484.

[8] O.A. Mezentsev, R. Zhu, R.E. DeVor, S.G. Kapoor, W.A. Kline, Use of radial forces for fault detection in tapping, International Journal of Machine Tools and Manufacture 42 (4) (2002) 479–488.

[9] Y. Altintas, P.K. Chan, In-process detection and suppression of chatter in milling, International Journal of Machine Tools and Manufacture 32 (3) (1992) 329–347.

[10] J.-J. Wang, C.M. Zheng, Identification of cutter offset in end milling without a prior knowledge of cutting coefficients, International Journal of Machine Tools and Manufacture 43 (7) (2003) 687–697.

[11] J.H. Ko, W.-S. Yun, D.-W. Cho, K.F. Ehmann, Development of a virtual machining system, Part 1: approximation of the size effect for cutting force prediction, International Journal of Machine Tools and Manufacture 42 (15) (2002) 1595–1605.

[12] W.-S. Yun, D.-W. Cho, Accurate 3-D cutting force prediction using cutting condition independent coefficients in end milling, International Journal of Machine Tools and Manufacture 41 (4) (2001) 463–478.

[13] K.A. Hekman, S.Y. Liang, In-process monitoring of end milling cutter runout, Mechatronics 7 (1) (1997) 1–10.

[14] D. Yan, T.I. El-Wardany, M.A. Elbestawi, A multi-sensor strategy for tool failure detection in milling, International Journal of Machine Tools and Manufacture 35 (3) (1995) 383–398.

[15] A.J. Stevens, S.Y. Liang, Runout rejection in end milling through two-dimensional repetitive force control, Mechatronics 5 (1) (1995) 1–13.

[16] S.Y. Liang, J.J. Wang, Milling force convolution modeling for identification of cutter axis offset, International Journal of Machine Tools and Manufacture 34 (8) (1994) 1177–1190.

[17] D.K. Baek, T.J. Ko, H.S. Kim, Optimization of feedrate in a face milling operation using a surface roughness model, International Journal of Machine Tools and Manufacture 41 (3) (2001) 451–462.

[18] S. Smith, J. Tlusty, An overview of modeling and simulation of the milling process, Transactions of the ASME: Journal of Engineering for Industry 113 (1991) 169–175.

[19] B.W. Ikua, H. Tanaka, F. Obata, S. Sakamoto, Prediction of cutting forces and machining error in ball end milling of curved surfaces–I, Theoretical Analysis. Precision Engineering 25 (4) (2001) 266–273.

[20] S. Ranganath, K. Narayanan, J.W. Sutherland, The role of flank face interference in improving the accuracy of dynamic force predictions in peripheral milling, Transactions of the ASME: Journal of Manufacturing Science and Engineering 121 (1999) 593–599.

[21] M.L. Campomanes, Y. Altintas, An improved time domain simulation for dynamic milling at small radial immersions, Transactions of the ASME: Journal of Manufacturing Science and Engineering 125 (2003) 416–422.

[22] X. Lui, M. Jun, R. DeVor, S. Kapoor, Cutting mechanisms and their influence on dynamic forces, vibrations and stability in micro-endmilling, in: Proceedings of the 2004 International Mechanical Engineering Congress and Exposition, November 13–20, Anaheim, CA; IMECE2004-62416.

[23] W.-M. Chau, Accuracy of milling operations based on dynamic models and simulation. M.S. Thesis, University of Florida, 1992.

[24] Y. Altintas, Manufacturing Automation, Cambridge University Press, Cambridge, UK, 2000.

[25] J. Tlusty, Manufacturing Processes and Equipment, Prentice-Hall, Upper Saddle River, NJ, 1999.

[26] Equipment manufacturers are specified for completeness. This does not imply endorsement by the authors.

[27] W. Nakkiew, C.W. Lin, J.F., A new method to measure runout of motorized end-milling spindles at very high speed rotations, in: Proceedings of the 18th Annual American Society for Precision Engineering 2003; October 26–31; Portland, OR (on CD).

[28] D.N. Dilley, Accuracy, vibration, and stability in drilling and reaming, D.Sc. Dissertation, Washington University in St. Louis, 2003.

[29] ASME B46.1-2002. Surface Texture, Surface Roughness, Waviness, and Lay, American Society of Mechanical Engineers, New York 2003.

[30] Y. Altintas, E. Budak, Analytical prediction of stability lobes in milling, Annals of the CIRP 44 (1) (1995) 357–362.

[31] M.A. Davies, J.R. Pratt, B. Dutterer, T.J. Burns, Stability prediction for low radial immersion milling, Transactions of the ASME: Journal of Manufacturing Science and Engineering 124 (2) (2002) 217–225.

[32] E. Budak, An analytical design method for milling cutters with nonconstant pitch to increase stability, Part 1: theory, Part 2: application, Transactions of the ASME: Journal of Manufacturing Science and Engineering 123 (2003) 29–38.

[33] H. Paris, G. Peigne, R. Mayer, Surface shape prediction in high speed milling, International Journal of Machine Tools and Manufacture 44 (2004) 1567–1576.